Composites Part B 199 (2020) 108268

Contents lists available at ScienceDirect

Composites Part B

journal homepage: www.elsevier.com/locate/compositesb

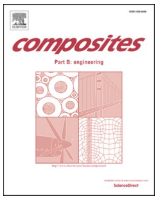

Enhancing strengthening efficiency of graphene nano-sheets in aluminum matrix composite by improving interface bonding

Z.Y. Liu [a], L.H. Wang [a], Y.N. Zan [a], W.G. Wang [b], B.L. Xiao [a,*], D. Wang [a], Q.Z. Wang [a], D.R. Ni [a], Z.Y. Ma [a,**]

[a] *Institute of Metal Research, Chinese Academy of Sciences, 72 Wenhua Road, Shenyang, 110016, China*
[b] *Liaoning Shihua University, 1 Dandong Road, Fushun, 113001, China*

ARTICLE INFO

Keywords:
Metal-matrix composites
Interface
Mechanical properties
Strength

ABSTRACT

Three 0.3 vol% graphene nano-sheet reinforced Al composites (GNS/Al), namely forged GNS/Al–4Cu, extruded GNS/Al–4Cu and forged GNS/Al–4Cu–1Mg, with different graphene-Al interfaces were prepared by wet mixing of graphene oxide aqueous solution and flaky Al powders, thermal reduction and subsequent powder metallurgy route. Their strengthening behaviors related with interface bonding were investigated, with the help of high resolution transmission electron microscopy, X-ray photoelectron spectroscopy and interface bonding test of specially designed model materials. In the forged composite, amorphous Al_2O_3 layer was observed between GNS and Al, resulting in a weak bonding of GNS and Al with interface shear strength of 117 MPa and normal strength of 227 MPa. In this case, nearly no strengthening effect was achieved by GNS addition. Using extruding to replace forging or adding Mg element could respectively break or exhaust amorphous Al_2O_3 layers, leading to improved graphene-Al interface bonding strength due to high fraction of Al–C ionic bond, thereby significantly increasing the strengthening effect of GNS. The best strengthening efficiency with a strengthening factor of ~33 was achieved in the forged GNS/Al–4Cu–1Mg due to strong interface shear strength of 209 MPa and normal strength of 402 MPa.

1. Introduction

Graphene (Gr) has attracted extensive interest as a potential reinforcement for aluminum matrix composites due to extremely high tensile strength (~30 GPa) and modulus (~1 TPa), which are similar to those for carbon nanotube [1–3]. Furthermore, its inherent two-dimensional morphology is more favorable for load transfer compared to fullerene and carbon nanotube. However, Gr is difficult to disperse into the aluminum matrixes effectively using traditional methods due to its large surface area and strong clustering tendency [4,5].

Some chemical processing routes, such as in-situ chemical vapor deposition [6–8] and molecular level mixing [9,10], have been proposed for effectively dispersing Gr in the metal matrixes with reduced structure damage of Gr. The resultant Gr/metal composites showed excellent strengthening effects. However, these methods are only suitable for Ni or Cu matrix, not for chemically active Al matrix. Furthermore, the capability of the above methods to scale up for bulk production has not been demonstrated. By comparison, ball milling is a convenient and effective method of dispersing carbon nanotubes into the aluminum matrixes [11–14]. It is also considered as an effective way for Gr reinforced Al (Gr/Al) composites. However, it is more difficult to balance the dispersion and structure damage of Gr during milling because of its two-dimensional morphology [15–18].

In recent studies, graphene oxide (GO)/Al powders were used as precursor to fabricate the Gr/Al composites [19–22]. It was reported that GO could be well dispersed into deionized water and adsorbed onto the Al powder surfaces to form the GO/Al composite powders. The GO/Al composite powders could be converted to graphene nano-sheet (GNS)/Al powders by subsequent chemical or thermal treatment. By using this method, uniform dispersion of GNS in the aluminum matrixes could be achieved.

Generally, native oxide of Al formed in the air or aqueous solution would impart a barrier layer between Al and GNS [19,20,23]. In this

---

* Corresponding author.
** Corresponding author.
E-mail addresses: blxiao@imr.ac.cn (B.L. Xiao), zyma@imr.ac.cn (Z.Y. Ma).

https://doi.org/10.1016/j.compositesb.2020.108268
Received 22 April 2020; Received in revised form 22 June 2020; Accepted 27 June 2020

case, there are two possible interfaces: Gr-Al_2O_3–Al and Gr-Al interfaces for the GNS/Al composites fabricated by this method. Although the Gr-Al interface could be well bonded during the hot-compaction at the fabrication temperature of the aluminum matrix composites [15,17,18,22], a much higher fabrication temperature was normally required for achieving well bonded Gr-Al_2O_3 interface [24]. Clearly, the load transfer through these two types of interfaces can be considerably different and would lead to significantly different strengthening efficiencies of GNS.

So far most of attentions have been focused on the fabrication methods [1,20,25–27], only a few investigations on the effect of interface bonding have been reported. For example, increased strengthening efficiency of GNS by interface reaction products of Al_4C_3 was reported [19]. However, Al_4C_3 was easy to hydrolyze in humid atmosphere, which was harmful to material application. Furthermore, most of the reported studies were essentially limited to the composites based on pure Al matrix [22,28]. Such composites are usually not attractive enough for applications due to their low strength.

In this study, the GNS/Al composite powders were prepared by wet mixing of GO aqueous solution and flaky Al powders. Three different fabrication procedures were respectively adopted to prepare GNS/Al–4Cu and GNS/Al–4Cu–1Mg composites with different types of interfaces. The microstructure and tensile properties of the above composites were investigated. The aims of this work are (a) to establish the optimum process for fabricating high strength GNS/Al composites and (b) to elucidate the relationship between interface bonding and strengthening efficiency of GNS in the GNS/Al composites.

2. Experimental

2.1. Fabrication of GNS/Al composite powders

GO (99% purity, mass ratio C:O = 2:1, Nanjing XF Nano Material Tech Co. Ltd., China) was added to deionized water and subsequently ultra-sonicated for 1 h to obtain dispersed GO aqueous solution with a concentration of 2 mg/ml. The morphology of the as-received GO and the GO in aqueous solution are respectively shown in Fig. 1(a) and (b). It can be seen that GO could be well dispersed in water after ultra-sonication (Fig. 1(b)), and the lateral sizes of most of GO with irregular shape were smaller than 3 μm, while the thickness of GO was smaller than 3 nm, indicating the layer number lower than 10.

200 g flake Al powders with a thickness of about 1 μm (Fig. 1(c)) were immersed into 30 vol% ethanol aqueous solution to form Al slurry. The GO aqueous suspension was quickly poured into the Al slurry and stirred for 1 min, and then the mixture was filtered and rinsed with ethanol. Finally, the wet GO/Al composite powders with 0.5 vol% GO were dried at 323 K and then treated at 773 K for 1 h under H_2 atmosphere to convert into nominal 0.3 vol% GNS/Al composite powders.

2.2. Fabrication of GNS/Al–4Cu and GNS/Al–4Cu–1Mg composites

Three different fabrication routes were respectively used to fabricate GNS/Al–4Cu and GNS/Al–4Cu–1Mg composites, as shown in Fig. 2.

2.2.1. Hot-forged GNS/Al–4Cu composite

The GNS/Al composite powders and Cu powders were mixed into the nominal GNS/Al–4Cu composite powders at 50 rpm for 8 h with a 1:1 ball to powder ratio, using a bi-axis rotary mixer. The as-mixed powders were cold-compacted in a cylinder die, degassed and hot-pressed at 853 K for 1 h into cylindrical billet with a diameter of 40 mm and a height of 58 mm. The billet was then hot forged into disc plate with a thickness of about 10 mm. The forged composite was solution treated at 773 K for 1 h, quenched into water and naturally aged for 4 days. For comparison, the corresponding Al–4Cu matrix alloy was also fabricated and heat-treated under the same conditions.

2.2.2. Hot-forged GNS/Al–4Cu–1Mg composite

The GNS/Al composite powders, Cu powders and Mg powders were mixed into the nominal GNS/Al–4Cu–1Mg composite powders. The other processes, including hot-pressing, hot-forging and heat treatment were the same as those for the hot-forged GNS/Al–4Cu composite in 2.2.1. For comparison, the corresponding Al–4Cu–1Mg matrix alloy was fabricated and heat-treated under the same conditions.

2.2.3. Hot-extruded GNS/Al–4Cu composite

Parts of the hot-pressed GNS/Al–4Cu composite and Al–4Cu billets were hot extruded at 693 K into bars with a diameter of 8 mm. The heat treatment was the same as that in 2.2.1.

2.3. Characterization of GNS/Al–4Cu and GNS/Al–4Cu–1Mg composites

The GNS distributions on the flaky Al powders were examined using field emission scanning electron microscopy (FE SEM, Leo Supra 55). The GNS distribution, Gr-Al interface and GNS structure were observed by transmission electron microscopy (TEM, Tecnai G2 20) and high resolution TEM (HRTEM, Tecnai G2 20). Flaky Al powders were dispersed in ethanol, diluted, dropped onto a Cu grid supported by carbon membrane with a thickness of 5 nm and then dried for TEM observation. Raman spectroscopic measurements were conducted using the JY Labram HR800 (excitation about 1 μm). The peak intensity (peak area) ratio of D-line (defect) and G-line (graphite), namely I_D/I_G was calculated to evaluate the disordering and defect density in graphitic structures. X-ray photoelectron spectroscopy (XPS) was used to obtain the chemical bonding information for three different GNS/Al composites. Fourier transform infrared (FTIR) spectrum of the GNS/Al composite samples (4000-600 cm^{-1}) were measured on a Thermo Scientific Nicolet 6700 infrared spectrometer.

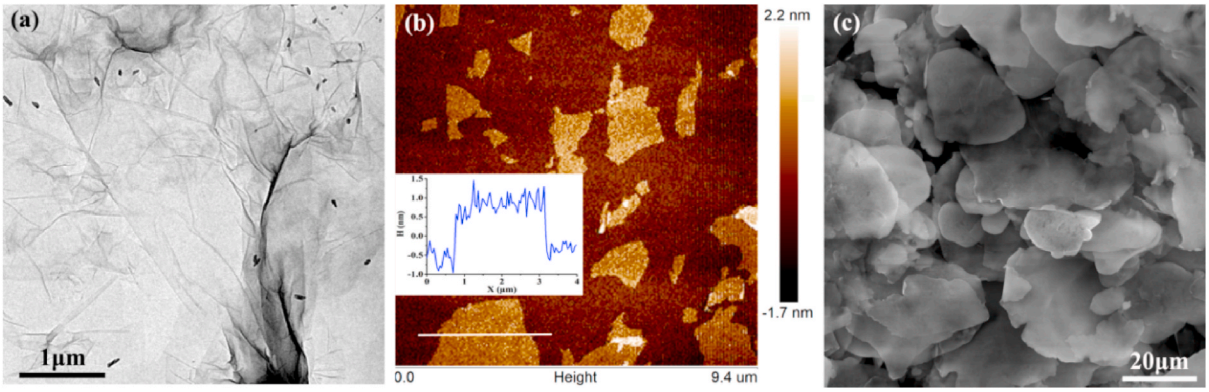

Fig. 1. Morphologies of (a) as-received GO, (b) dispersed GO, and (c) flaky Al powders.

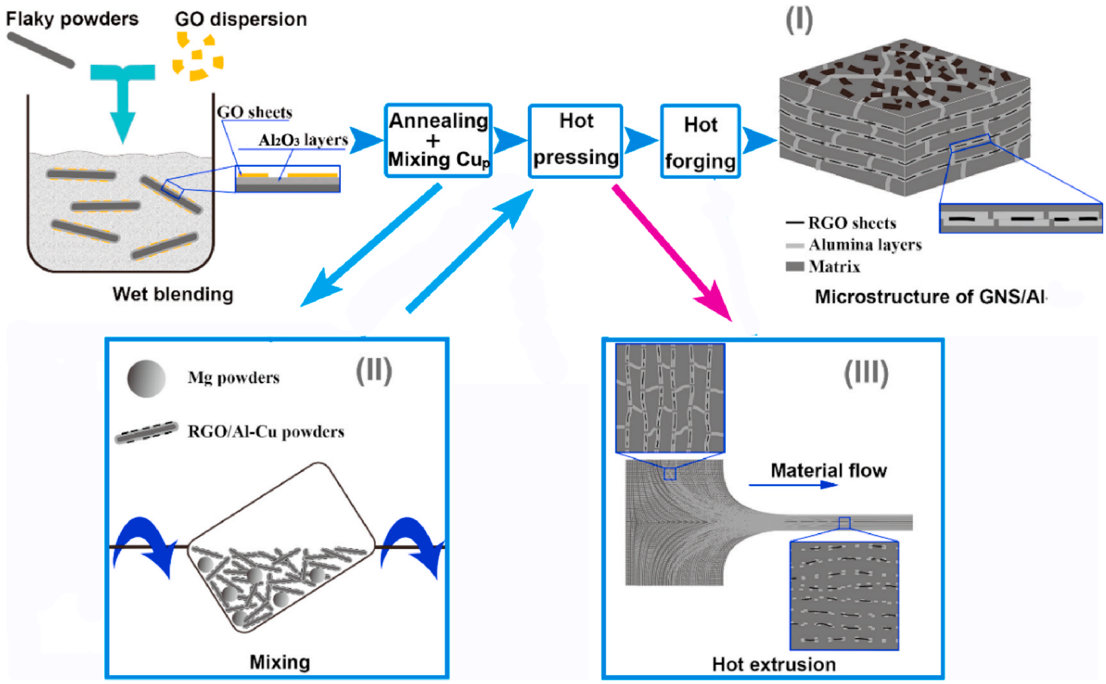

Fig. 2. Schematic of three fabrication routes: (I) forging, (II) adding Mg element and (III) extrusion.

Tensile specimens with a gauge length of 5 mm, a width of 1.5 mm, and a thickness of 1 mm were respectively machined from the extruded composite parallel to the extruding direction and from the forged composites parallel to the radius direction. Tensile tests were conducted at a strain rate of 1×10^{-3} s^{-1} at room temperature using an Instron 5848 microtester. At least five specimens were tested for each composite. The fracture surfaces of the composites were observed using FESEM (Leo Supra 55).

2.4. *Al/Gr/Al model materials for interface strength evaluation*

For evaluating the strengths of the Gr-Al interface, Al/Gr/Al model materials were fabricated, as shown in Fig. 3. Gr films (4–8 layers) fabricated by chemical vapor deposition were provided by Chengdu Organic Chemicals Co. Ltd., China. The diameter and height of Al–4Cu block were respectively 30 and 20 mm. A Gr film was transferred onto the clean-smooth surface of one Al–4Cu block. Then, another Al–4Cu block with clean-smooth surface was stacked onto the Al–4Cu block covered by the Gr film, followed by hot-pressing at 853 K for 1 h in vacuum at an applied pressure of 80 MPa to obtain Al–4Cu/Gr/Al–4Cu model material. Similarly, Al–4Cu–1Mg/Gr/Al–4Cu–1Mg and Al–4Cu/Al–4Cu model materials were also fabricated in the same way.

Just the same as the Al powder, the surface of Al block would naturally form a layer of alumina film. It was reported that the natural oxidation of fresh aluminum surface is a self-limiting growth process, and its thickness is relatively stable at room temperature, generally around 10 nm [29]. Furthermore, the model materials underwent the same thermal-pressure history as the composites, which would result in the similar Gr-Al interface structures as those for the GNS/Al composites. In theory, the Gr-Al interface strength measured by the model materials could reflect the interface bonding in the GNS/Al composites. XPS was used to obtain the chemical bond information for the Al/Gr/Al model materials, for confirming the fracture position of the model materials and comparing the interface chemical bonds with the GNS/Al composites.

For the model materials, it is difficult to accurately determine the position of Gr, because of the extremely thin thickness of Gr. Thus, the interface shear strength was evaluated by a tensile test with pure shear fracture rather than a classical shear test. Tensile specimens with a gauge length of 10 mm, a width of 1.5 mm, and a thickness of 1.2 mm were machined from the model materials with an off-axis angle of 45° or 90° to the Gr films for achieving maximum shear stress along the Gr-Al interface or maximum normal stress perpendicular to the Gr-Al interface during tension. The larger gauge length of 10 mm rather than 5 mm was used to ensure that the Gr-Al interface was within the gauge length. Tensile tests were conducted at a strain rate of 1×10^{-3} s^{-1} at room temperature. Finally, interface shear strength ($[\tau]$) and normal strength ($[\sigma]$) were respectively calculated by tensile strength for the specimens with pure shear fracture and normal fracture at the Gr-Al interface.

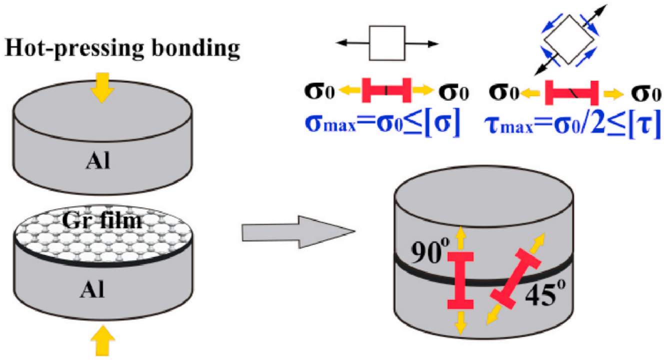

Fig. 3. Fabrication route of Al/Gr/Al model materials and tensile testing schematic for determining interface shear and normal strength.

3. Results

3.1. *Characterization of GNS/Al composite powders*

Fig. 4(a) and (b) show the Raman spectra of the GO/Al composite powders before and after annealing treatment. The I_D/I_G ratio decreased from 2.21 to 1.74 for the composite powders after annealing at high temperature. This indicates that the graphite structure was recovered after annealing. Previous investigations indicated that GO could be

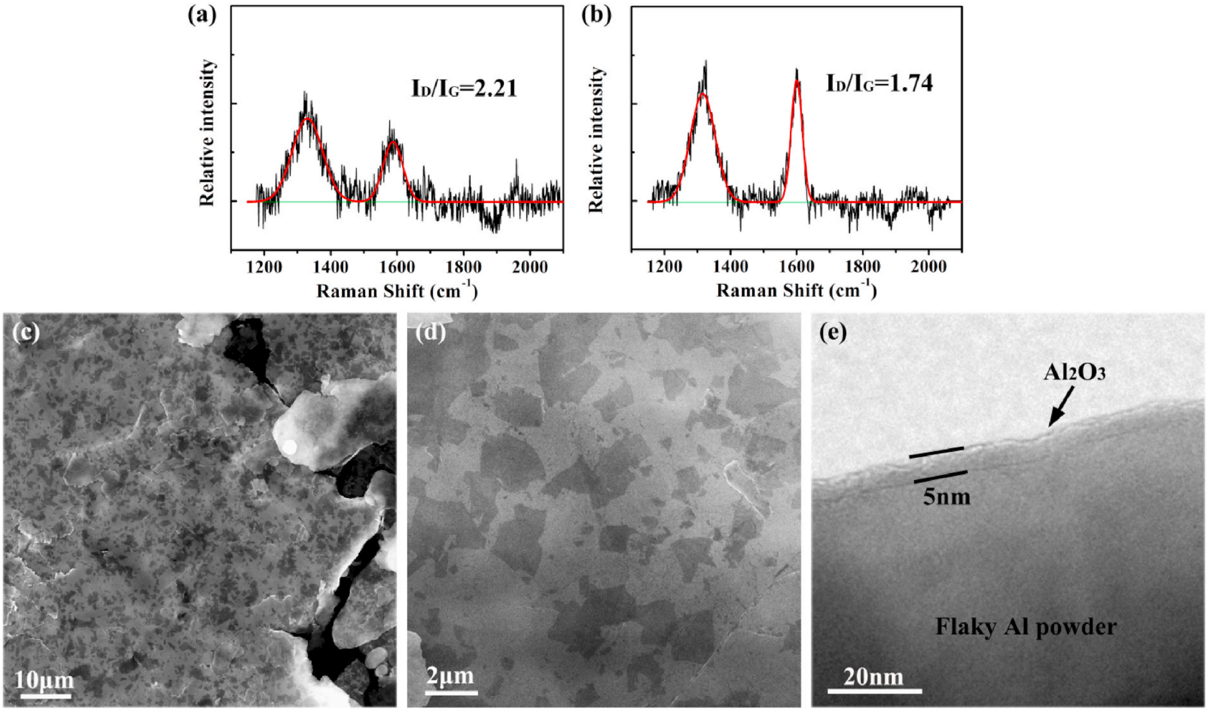

Fig. 4. Raman spectra of (a) GO/Al powders and (b) GO/Al powders annealed at 773 K for 1 h; (c) and (d) FE-SEM images showing GNS distributions on flaky Al powders after annealing treatment, (e) TEM image showing amorphous Al_2O_3 on flaky Al powders in 0.3 vol% GNS/Al composite powders.

converted into GNS during annealing treatment around 673–823 K under Ar or H_2 atmosphere [9,19,20], as the result of the decomposition of oxide groups and re-bonding of C–C bonds. Therefore, the annealing temperature of 773 K in this study was able to convert GO into GNS in the GO/Al powders.

Fig. 4(c) and (d) show the GNS distributions in the GNS/Al composite powders. Uniformly dispersed GNS with lateral sizes of about 0.4–2 μm were adsorbed on the flaky Al powders, mainly due to the electrostatic adsorption effect of Al and precursor GO, which was reported in a previous investigation using the same dispersion method [23]. No micro-pores or re-agglomerations of GNS were observed for the GNS/Al powders after annealing treatment (Fig. 4(d)). This could be attributed to two reasons. Firstly, the as-received GO had a relatively large mass ratio of C/O. This means that the structure defect density was relatively low after thermal reduction of GO. Secondly, because GO flakes were adsorbed on the flaky Al powders, the adsorption forces could effectively constrain the movement of GO as it changed to GNS.

An amorphous Al_2O_3 layer with a thickness of about 5 nm was observed on the surface of the flaky Al powders, as shown in Fig. 4(e). The surface oxidation of the Al powders is a quick and spontaneous process as Al exposed to air or wet atmosphere. Therefore, an amorphous Al_2O_3 layer was formed on the Al powders, though the mixing duration was very short. In the hot pressing, the amorphous Al_2O_3 layer on the flaky Al powders could become a barrier layer between Al and GNS, which would affect the bonding between GNS and Al.

3.2. *Microstructure of GNS/Al composites*

Microstructures of the hot-forged 0.3 vol% GNS/Al–4Cu composite are shown in Fig. 5(a–c). Strip-shaped phases were uniformly and directionally dispersed, with their axis perpendicular to the forging direction (Fig. 5(a)). The magnified view shown in Fig. 5(b) demonstrated that the strip-shaped phases consisted of GNS and Al_2O_3 distributed on the surface of GNS. HRTEM image indicated that the layer structure of GNS was well retained (Fig. 5(c)), with the GNS layer number smaller than 10 and the layer distance being about 0.33 nm, which was in accordance with that of graphite.

Fig. 5(c) also shows that the Al_2O_3 layers distributed on the surface of GNS had a thickness of about 5 nm, consistent with the result shown in Fig. 4(e). It is believed that for the hot-forged GNS/Al–4Cu composite, the Al_2O_3 layers on the surface of flaky Al powders could not be fully fractured, because of the small deformation ratio of forging. More importantly, GNS could play a role of armor for the Al_2O_3 layers during deformation. As a result, the Al_2O_3 layer between GNS and Al matrix could still retain its complete morphology after forging (Fig. 5(c)).

Fig. 5(d–f) shows the microstructures of hot extruded GNS/Al–4Cu composite. Elongated grains and many small Al_2O_3 particles were observed in the composite (Fig. 5(d)). No GNS with a large size similar to that in Fig. 5(a) could be observed. Magnified view indicated that GNS were aligned along the extrusion direction and uniformly distributed in the matrix (Fig. 5(e)). A few of GNS pieces with much smaller dimensions (~100 nm) were also observed in the extruded composite, which were not found in the forged GNS/Al–4Cu composite. Some of the Gr-Al interfaces without amorphous Al_2O_3 intermediate layers were observed, as shown in Fig. 5(f). This indicates that the large deformation of hot extrusion could partly fracture the Al_2O_3 and GNS, thereby forming the direct Gr-Al bonding.

The fracture of reinforcements during plastic deformation with a large deformation ratio was a common phenomenon for the aluminum matrix composites, e.g. carbon nanotube/Al composites [30,31]. In this study, although the lateral dimension of GNS was significantly reduced during hot extrusion, the layer structure of GNS was not destroyed (Fig. 5(f)). It was reported that carbon nanotube and Al could form well bonding during hot deformation [32]. This implies that the direct Gr-Al contact could also form a good bonding during hot extrusion, considering the similar structure of GNS and carbon nanotube.

The microstructures of the hot-forged GNS/Al–4Cu–1Mg composite are shown in Fig. 5(g and h). By adding 1 wt% Mg, the Al_2O_3 layers were consumed with the direct contact of Al and GNS being obtained (Fig. 5(h)) and $MgAl_2O_4$ particles formed in the composite (Fig. 5(g)). Furthermore, the HRTEM verified that the layer structure of GNS was also well retained (Fig. 5(h)). More importantly, no Al_4C_3 was detected

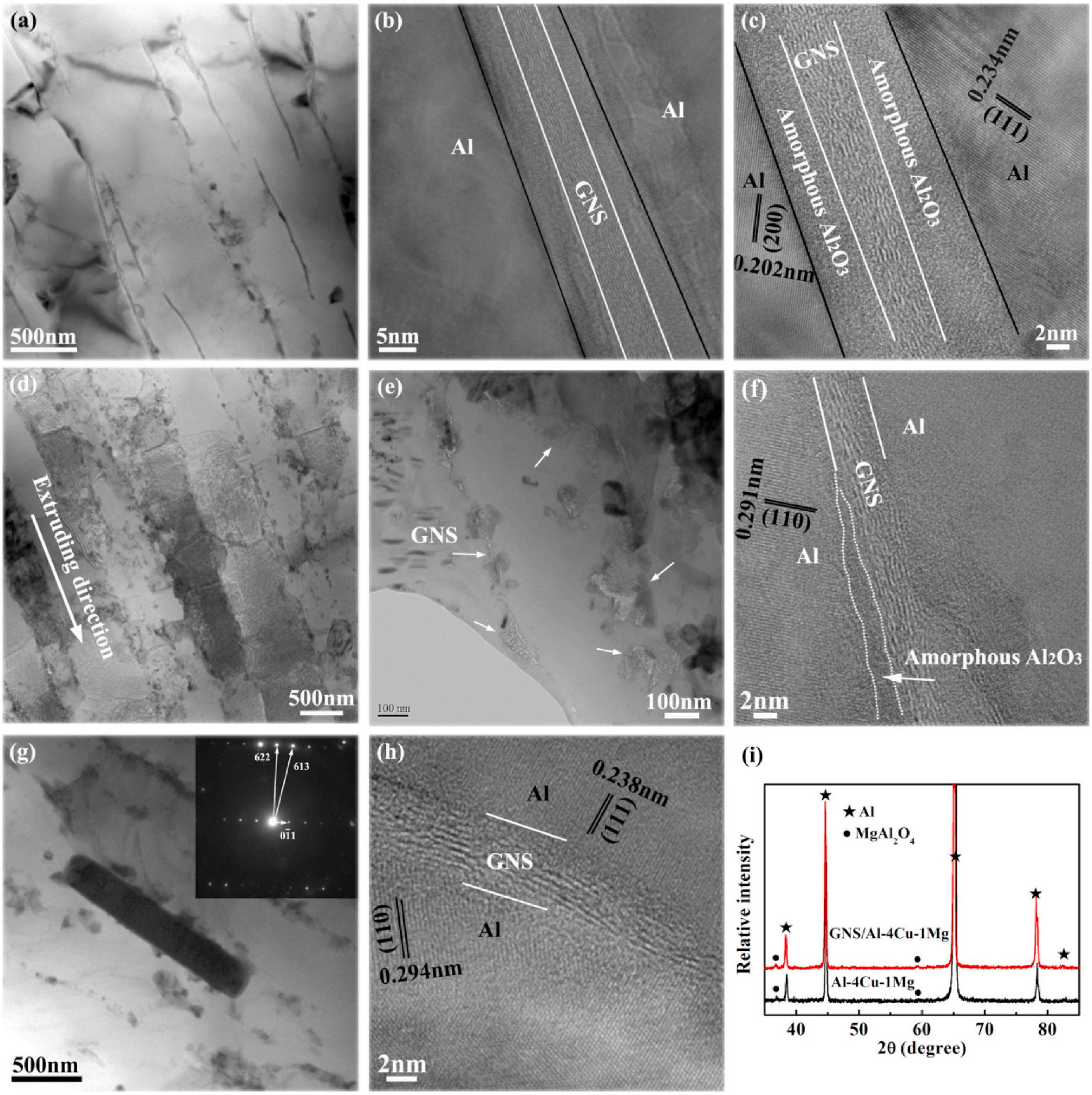

Fig. 5. TEM and HRTEM images showing (a) GNS distribution, (b) and (c) Gr-Al interface in hot-forged GNS/Al–4Cu composite; (d) (e) GNS distribution and (f) Gr-Al interface in hot extruded GNS/Al–4Cu composite; (g) formation of $MgAl_2O_4$ and (h) Gr-Al interface in hot-forged GNS/Al–4Cu–1Mg composite; (i) XRD patterns of Al–4Cu–1Mg and GNS/Al–4Cu–1Mg composite.

under HRTEM or XRD (Fig. 5(i)), though Al and GNS directly contacted.

According to Fig. 4(e), a layer of Al_2O_3 with a thickness of about 5 nm existed on the surface of the flaky Al powder. By adding Mg element, the transient liquid phase rich in Mg element would appear in the hot pressing process. The transient liquid phase diffused rapidly along the powder boundaries and contacted with Al_2O_3. Simultaneously, Mg could react with Al_2O_3 as follows [33]:

$$Al_2O_3+3\ Mg = 3MgO+2Al\ \Delta G = -128449 + 11.5T \tag{1}$$

$$MgO + Al_2O_3 = MgAl_2O_4\ \Delta G = -33890 + 2.6T \tag{2}$$

The negative Gibbs energy values for Reactions (1) and (2) confirm the feasibility for the reaction consumption of Al_2O_3 and the formation of $MgAl_2O_4$. It is reported that in situ $MgAl_2O_4$ spinel can be formed at relatively low temperatures (~833 K) using oxygen-supplying sources in aluminum alloys [34].

The thickness of Al_2O_3 and flaky Al powders were respectively about 5 and 1000 nm. This means that the Al_2O_3 concentration in the total Al matrix was about 1 vol% (1.4 wt%). According to Reactions (1) and (2), 1 wt% Mg could consume 5.7 wt% Al_2O_3. This indicates that Mg could exhaust all the Al_2O_3 and about 0.7 wt% Mg could be retained. XRD patterns shown in Fig. 5(i) also verified the disappearance of Al_2O_3 and existence of $MgAl_2O_4$ in the unreinforced alloy and composite with the Mg element addition. As Al_2O_3 could be totally exhausted by reaction with Mg, the direct contact between Al and GNS were obtained (Fig. 5 (h)).

3.3. Tensile properties of GNS/Al composites

Fig. 6(a)(b) show typical tensile curves, and Table 1 shows tensile properties of the GNS/Al composites fabricated in different routes. For the forged materials, yield strength (YS) and ultimate tensile strength (UTS) of the Al–4Cu alloy were respectively 198 and 369 MPa, while YS and UTS of the GNS/Al–4Cu composite were respectively 196 and 362 MPa. Clearly, no strength increase was achieved by GNS incorporation.

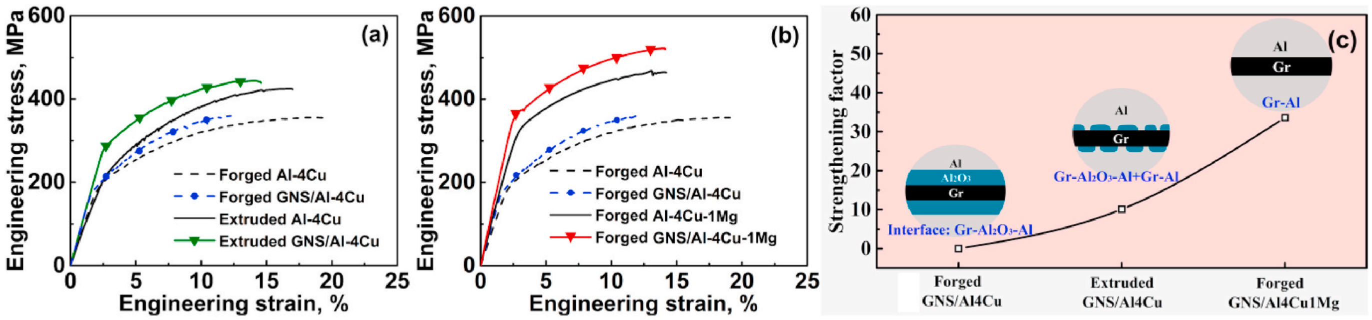

Fig. 6. (a) (b) Typical tensile curves of different composites and corresponding matrix alloys; (c) Strengthening factors of different composites.

Table 1
Tensile properties of GNS/Al composites and unreinforced alloys fabricated in different routes.

States	Materials	YS (MPa)	UTS (MPa)	El (%)
Hot-forged + T4	Al–4Cu	198 ± 7	369 ± 8	14 ± 1
	GNS/Al–4Cu	196 ± 8	362 ± 9	9 ± 2
Hot-extruded + T4	Al–4Cu	229 ± 5	427 ± 5	11 ± 0.5
	GNS/Al–4Cu	281 ± 7	440 ± 8	10 ± 0.5
Hot-forged + T4	Al–4Cu–1Mg	305 ± 6	456 ± 8	9 ± 1
	GNS/Al–4Cu–1Mg	355 ± 5	502 ± 10	9 ± 1

For the extruded materials, YS and UTS of the Al–4Cu alloy were respectively 229 and 427 MPa, while YS and UTS of the GNS/Al–4Cu composite were respectively 281 and 440 MPa. It can be seen that the extruded Al–4Cu alloy exhibited considerably increased strength compared to the forged one. More importantly, GNS incorporation resulted in an increase in both YS and UTS of the extruded Al–4Cu.

For the forged materials with 1 wt% Mg addition, the strengths of Al–4Cu–1Mg alloy were much higher than those of the forged and extruded Al–4Cu alloys, mainly due to strengthening of residual Mg alloying. For the forged GNS/Al–4Cu–1Mg composite, both YS and UTS were increased by about 50 MPa compared with those for the Al–4Cu–1Mg alloy. A more interesting thing was that the elongation of the composite was not reduced compared with that of the matrix alloy.

4. Discussion

4.1. Modelling analysis on strength

As previously suggested, the strength of metal matrix composites (σ_c) can be expressed based on the following equation [21,35,36]:

$$\sigma_c = \sigma_m(1 + V_f R) \tag{3}$$

where *R* is the strengthening factor of the reinforcement, V_f is the volume fraction of reinforcement, and σ_m is the strength of the matrix. The strengthening factor *R* reveals the efficiency of strength improvement due to reinforcement incorporation.

Fig. 6(c) shows the strengthening factors for different composites. The composite with Mg addition had the highest strengthening factor of ~33, while the extruded and forged GNS/Al–4Cu composites had strengthening factors of ~10 and ~0, respectively. For evaluating the effect of the interface on the strengthening, a highly accurate model should be used.

Shin et al. [37] proposed a model to predict strength of nano-carbon/metal composites based on analysis of efficiency parameters in which interface feature was strongly emphasized, and the strength of the composite could be expressed as:

$$\sigma_c = \sigma_m(1 - V_f) + c(kgs)\sigma_f V_f \tag{4}$$

where c is an empirical constant, *k* is the bonding factor, *g* is the geometry factor of the reinforcements, s is the alignment factor of reinforcements.

$$k = \frac{aE_{vander,Al-C} + bE_{ionic,Al-C}}{E_{total,Al-C}} \tag{5}$$

where *a* and *b* are the volume fraction of Al–C van der Waals and ionic bonds, $E_{vander,Al-C}$ and $E_{ionic,Al-C}$ are the van der Waals (0.54 ev) and ionic bonding (4.4 ev) energy of Al–C bonds, respectively. Eqs. (4) and (5) indicate that high volume fraction of Al–C ionic bonding is beneficial to achieve strong interface bonding and high strengthening efficiency.

The chemical bonding features of the hot-forged GNS/Al–4Cu and GNS/Al–4Cu–1Mg composites were examined by FTIR, as shown in Fig. 7. For the hot-forged GNS/Al–4Cu composite (Fig. 7(a)), the characteristic peaks of Gr were observed for C–O–C stretching vibration at 1125 cm^{-1}, C sp^2 stretching vibration from 1550 to 1650 cm^{-1}, and C=O stretching vibration at about 1750 cm^{-1}. The characteristic peaks of Al_2O_3 were observed at 2950 cm^{-1}, 1350-1500 cm^{-1}, while a wide adsorption band were observed below 1000 cm^{-1}, which was the typical characteristic of nano-sized Al_2O_3 (n-Al_2O_3). In addition, the absorption peaks at 3400 cm^{-1} were produced from –OH stretching vibration in Gr or adsorbed H_2O on the surface of Al_2O_3. For the hot-forged GNS/Al–4Cu–1Mg composite (Fig. 7(b)), the Gr and $MgAl_2O_4$ characteristic peaks were detected, which was in accordance with the microstructures shown in Fig. 5(g–i). An interesting phenomenon is that the C–O–C peak was significantly weakened, while the –OH and n-Al_2O_3 characteristic peaks totally disappeared due to Mg addition. However, no pronounced Al–C peak (~750 cm^{-1}) could be detected for either hot-forged GNS/Al–4Cu or GNS/Al–4Cu–1Mg composites, resulting from the low concentration of Gr in these composites.

The Al–C bonding features were examined by XPS measurements, as shown in Fig. 8. Al–C, C–C, Al–O bonds and Al metallic bond were detected, whilst residual C–O bond (with small peak area) of reduced GO was also observed. A quantitative portion of ionic bonds in the composites was calculated with the area underneath the peaks for Al–C ionic bonds, Al metallic bonds and C–C covalent bonds. The fraction of a certain bond consisting of A and B (X_{A-B}), and bonding fraction of Al–C bond (BF_{Al-C}) can be calculated as follow [37,38]:

$$X_{A-B} = \frac{S_{A-B} \cdot N \cdot V}{S_{A-B} \cdot N \cdot V + S_{B-B} \cdot \frac{M_B}{\rho_B}} \tag{6}$$

$$BF_{Al-C} = \frac{X_{Al-C} + X_{C-Al}}{X_{Al-C} + X_{C-Al} + X_{Al} + X_C} \tag{7}$$

where *N* is the Avogadro number, *M* is the atomic mass, *ρ* is the density, *V* is the unit cell volume fraction, and *S* is the peak area for different bonds in XPS spectra.

The bonding fractions of Al–C for the hot-forged GNS/Al–4Cu, hot-extruded GNS/Al–4Cu and hot-forged GNS/Al–4Cu–1Mg calculated by Eqs. (6) and (7) were 9.2%, 12.6% and 17.5%, respectively. It is believed that the existence of Al_2O_3 between Al and GNS led to the low fraction of

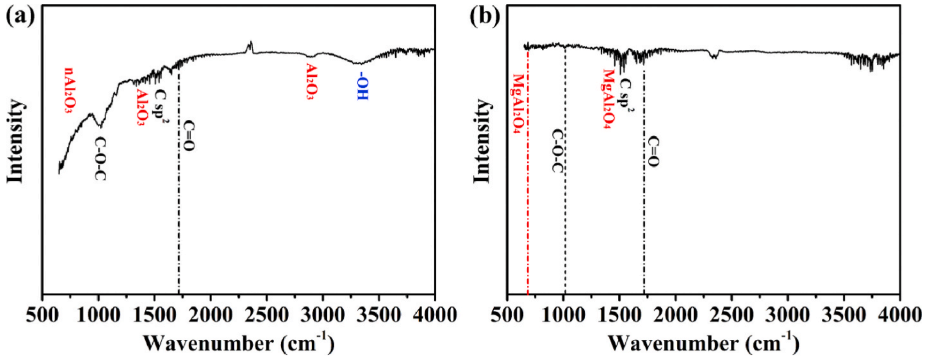

Fig. 7. FTIR spectra for different GNS/Al composites: (a) hot-forged GNS/Al–4Cu, (b) hot-forged GNS/Al–4Cu–1Mg.

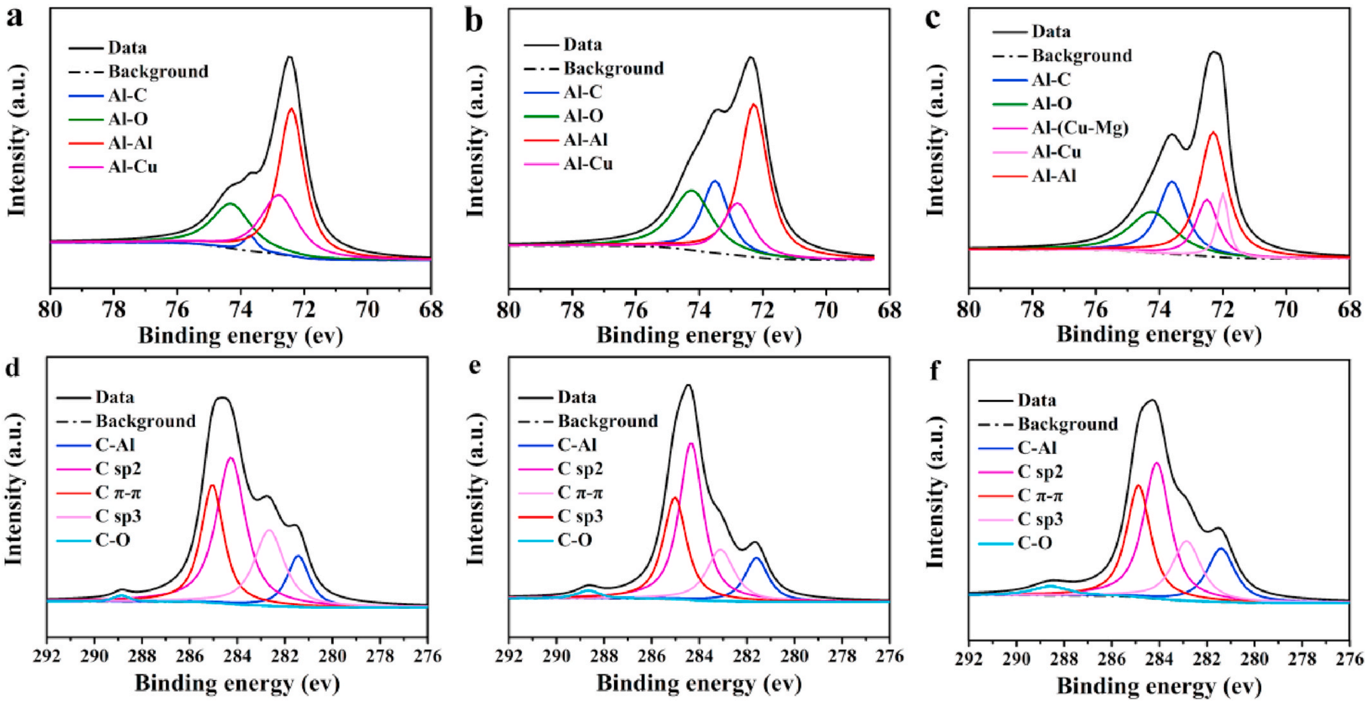

Fig. 8. XPS spectra for different GNS/Al composites: (a) (d) hot-forged GNS/Al–4Cu, (b) (e) hot-extruded GNS/Al–4Cu and (c) (f) hot-forged GNS/Al–4Cu–1Mg.

Al–C ionic bonding, and the Al–C ionic bonding fraction increased due to the rupture or reaction consumption of Al_2O_3. It means that the interface bonding strength of Gr-Al for the hot-forged GNS/Al–4Cu–1Mg and hot-forged GNS/Al–4Cu should be the strongest and weakest, respectively, according to Eqs. (4) and (5).

4.2. Interface bonding strength testing based on model materials

For verifying the above interface bonding behaviors and obtaining the interface strength of the three GNS/Al composites, the Al/Gr/Al model materials were designed, and corresponding interface shear and normal strengths were specially tested, as shown in Figs. 9 and 10. The interface shear strengths [τ] of Al–4Cu/Al–4Cu, Al–4Cu/Gr/Al–4Cu and Al–4Cu–1Mg/Gr/Al–4Cu–1Mg model materials were respectively 142, 117 and 209 MPa. The interface normal strengths [σ] of Al–4Cu/Al–4Cu, Al–4Cu/Gr/Al–4Cu and Al–4Cu–1Mg/Gr/Al–4Cu–1Mg model materials were respectively 274, 227 and 402 MPa.

Until now, the knowledge of the interlayer shear strength of Gr was unexpectedly confused. According to general understanding, the interlayer bonding of graphite was considered to relatively weak. For example, the interlayer shear strength was tested to be only 140 MPa for single crystalline graphite with a thickness of about 500 nm using a shearing off testing [39]. However, Bonelli et al. [40] and Guo et al. [41] respectively obtained interlayer shear strengths of 434 MPa and 900 MPa by tight-binding atomistic simulation. Ding et al. [42] even obtained an interlayer shear strength of 2 GPa for highly oriented pyrolytic graphite using the method of STM/AFM, and attributed this high value to nano-scale structure hardening as the result of the suppression of dislocation activity. In our study, the Gr delamination was not found even in the Al–4Cu–1Mg/Gr/Al–4Cu–1Mg model material with higher strength, which could also be reflected by the quite different tensile data of the three model materials. This could be attributed to the difficulty for dislocation activation as the result of the fewer layer of Gr (<10), and it also indicated that the interface bonding testing would not be significantly affected by interlayer sliding of Gr.

Fig. 11 shows the typical XPS spectra of the fracture surfaces of the Al/Gr/Al model materials after tension. Obviously, C 1s, O 1s as well as Al 2p peaks were identified in the XPS survey spectra (Fig. 11(a)(d)). It indicates that the model materials actually fractured at the position of Gr-Al interface, thereby verifying the effectiveness of the interface bonding strength. Compared with those of the GNS/Al composites, the XPS spectra of the Al/Gr/Al model materials had much higher fraction of

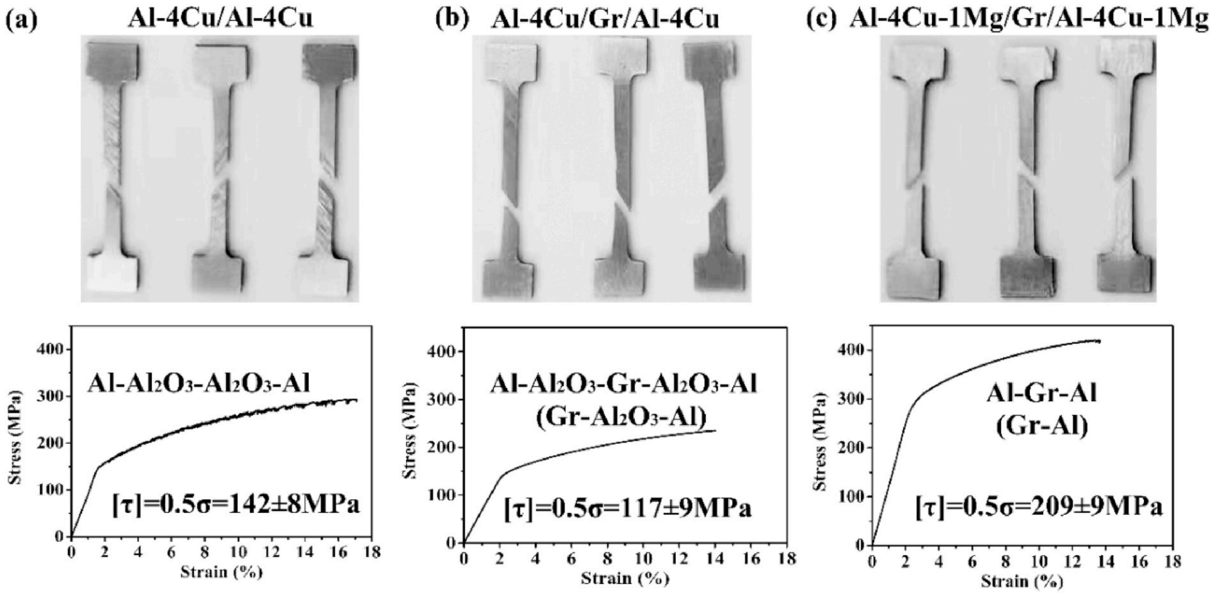

Fig. 9. Typical failed tensile specimens of model materials with pure shear fracture and typical tensile curves for interface shear strength tests.

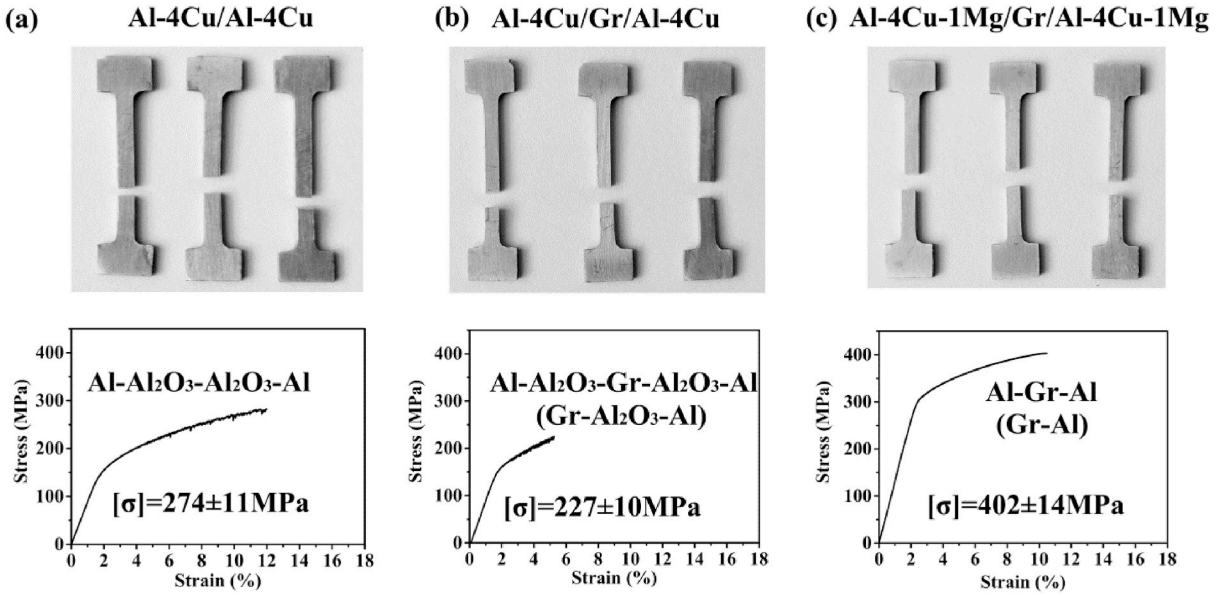

Fig. 10. Typical failed tensile specimens of model materials with normal fracture and typical tensile curves for interface normal strength tests.

Al–O and Al–C bonds (Fig. 11(b, c, e, f)). This is because the model materials were not uniform-structured, and the Gr or Al_2O_3 were merely distributed at the fracture position and led to high concentration of Gr or Al_2O_3. Nevertheless, the types of chemical bonds on the fracture surfaces of the model materials were similar with those of Gr-Al interfaces in the GNS/Al composites, which indicated that the interface bonding testing of the model materials was reasonable for understanding the GNS/Al composites.

For the Al–4Cu/Al–4Cu model material, a natural layer of amorphous Al_2O_3 formed on the surface of Al, and thus, the Al–Al_2O_3–Al_2O_3–Al interface shear and normal strength were considered to be about 142 and 274 MPa, respectively. Similarly, the Al–Al_2O_3-Gr-Al_2O_3–Al (considering symmetry, labelled as Gr-Al_2O_3–Al) interface shear and normal strength could be considered to be respectively 117 and 227 MPa, much lower than that of Al–Al_2O_3–Al_2O_3–Al interface. This indicates that good Gr-Al bonding could not be obtained due to the existence of amorphous Al_2O_3 layer.

Because of high melting point of ceramic, good bonding of ceramic-ceramic needs a much higher temperature, e.g. at least ~1573 K for GNS/Al_2O_3 composites to achieve a strong bonding of Gr-Al_2O_3 [24,43]. However, the hot compacting temperature for the model composites were only about ~853 K in this study, much lower than the temperature for forming good bonding of Gr-Al_2O_3 interface. This is why the Al–Al_2O_3-Gr interfaces were weakly bonded. For comparison, the interface shear and normal strength for Al–4Cu–1Mg/Gr/Al–4Cu–1Mg model material were as high as ~209 and 402 MPa, respectively. Because Mg could exhaust the amorphous Al_2O_3 film (Fig. 5(h)), direct Al-Gr-Al (considering symmetry, labelled as Gr-Al) bonding with high strength could be achieved. These above mentioned interface bonding strength results are consistent with the result of XPS.

4.3. Strength analysis based on interface bonding

For the forged GNS/Al–4Cu composite, the existence of amorphous

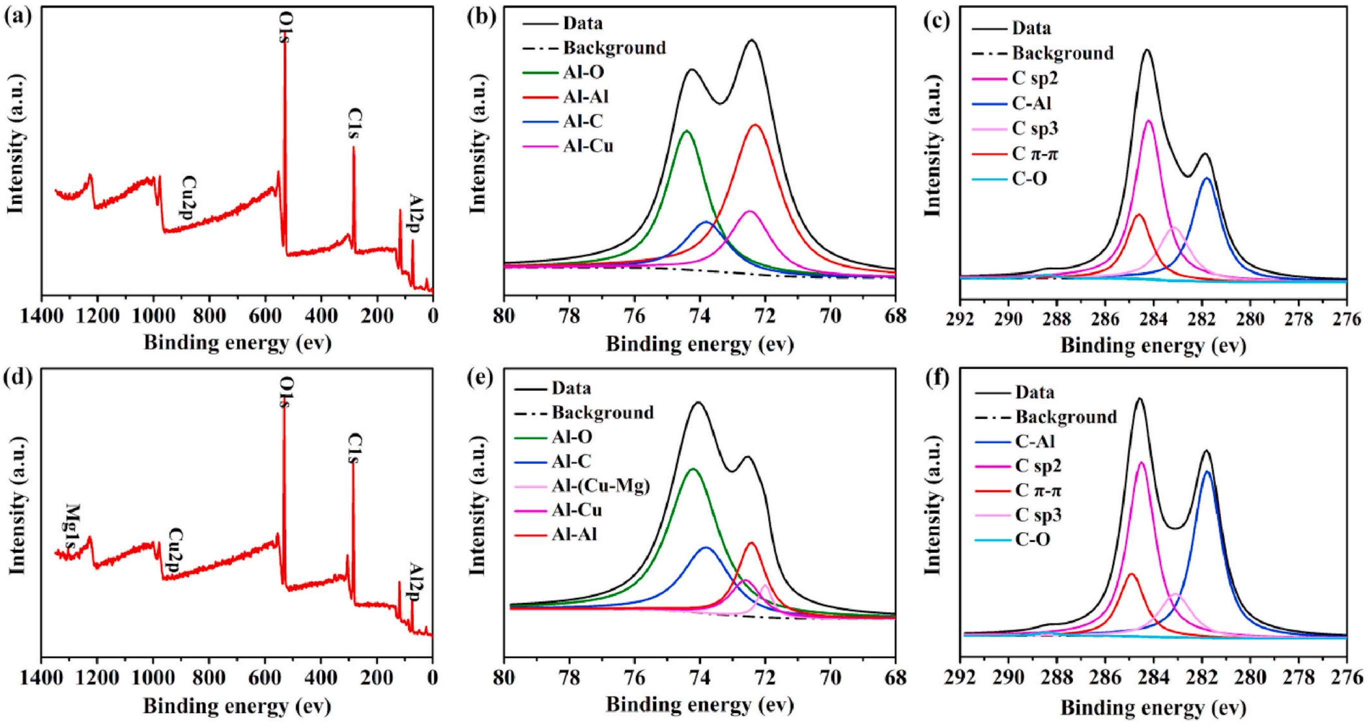

Fig. 11. XPS spectra for the fracture surface of Gr/Al/Gr model materials: (a) (b) (c) Al–4Cu/Gr/Al–4Cu, (d) (e) (f) Al–4Cu–1Mg/Gr/Al–4Cu–1Mg.

Al_2O_3 intermediate layer between GNS and Al led to a low fraction of Al–C bond. It was reported that the strengthening efficiency of Gr was directly related to the fraction of Al–C, Al–O–C ionic bonds in Gr/Al composite [37]. However, according to XPS results in Fig. 8, the Al–O–C ionic bond fraction was very small and thus the strengthening efficiency of Gr was determined by Al–C ionic bond fraction. According to Eqs. (4)–(7), the stress could not be effectively transferred due to the low Al–C ionic bond fraction. The significantly reduced strengthening was in accordance with the quite different strengthening factors of Gr/Al and Gr/Ti composites due to the differences in their Metal-C ionic bond fraction [37]. Further, according to the interface bonding strength testing, the Gr-Al bond strength ([τ]~117 MPa, [σ]~227 MPa) of the corresponding model material was even a little lower than that of the matrix. As a result, no obvious strengthening was achieved for the forged GNS/Al–4Cu composite.

It should be mentioned that Gr showed a beneficial effect on the tensile strength of pure Al matrix composites at high temperature in our previous investigation [44]. This is not contradictory to the viewpoint of the weakening effect of Al_2O_3 on the Gr-Al interface. On one hand, the strength of pure Al matrix was relatively low, much lower than 200 MPa. On the other hand, the pure Al matrix would further soften at high temperature. This means that the Gr-Al_2O_3–Al interface bonding strength was high enough to achieve strengthening at high temperature. However, for the Al–4Cu matrix with much higher strength than pure Al, the strength of Gr-Al_2O_3–Al interface bonding was lower than that of the matrix, thereby exhibiting no obvious strengthening.

After extrusion, part of direct Gr-Al bonding were formed as continuous Al_2O_3 layers were broken up, and therefore strengthening factor increased. However, there were still many weakly bonded Gr-Al interfaces with amorphous Al_2O_3 intermediate layer, and furthermore, GNS dimensions were reduced after extrusion (Fig. 5(e)), which was not beneficial to transferring load. In general, extrusion could align reinforcements and was beneficial to achieve higher tensile strength along the extrusion direction. As shown in Fig. 5, GNS were all well aligned along the tension direction for the three composites, GNS orientation would not lead to strength difference. As a result, the strengthening factor for the extruded composites was only increased to ~10.

For the forged GNS/Al–4Cu–1Mg composite, the amorphous Al_2O_3 layers were totally exhausted by the added Mg. Therefore, a direct bonding of Gr-Al with high bonding fraction of Al–C bond and high interface strength ([τ]~209 MPa, [σ]~402 MPa) were formed, and stress could be effectively transferred through the interface. As a result, a much higher strengthening factor of ~33 was achieved for the GNS/Al–4Cu–1Mg composite.

Fig. 12 shows the fractographs of various composites. For the forged GNS/Al–4Cu, both dimple and intergranular fracture could be observed on the fracture surfaces (Fig. 12(a)). The intergranular fracture characteristic means the weak Al–Al bonding. At the bottom of the dimples, GNS with large lateral sizes were pulled-out from the matrix with tearing interfaces (Fig. 12(b)). In addition, no Al matrix was adhered to the pulled-out GNS. This proves that the bonding of Gr-Al interface with amorphous Al_2O_3 intermediate layer was poor.

According to Fig. 5(b) and (c), a Al_2O_3 layer existed between Al and GNS. As the temperature for hot-pressing (853 K) was too low for forming good bonding for the Al_2O_3-Gr interface [24,43], the load transfer through the Gr-Al interface with amorphous Al_2O_3 intermediate layer was not efficient. Furthermore, the deformation during hot forging was not severe enough for breaking the Al_2O_3 layer, which means that no direct contact of Gr-Al could be achieved. Therefore, intergranular fracture was observed and many pulled-out GNS with tearing interface were found at the bottoms of dimples on the fracture surface (Fig. 12 (b)).

For the fractographs of the forged GNS/Al–4Cu–1Mg and hot-extruded GNS/Al–4Cu, obvious dimples rather than intergranular fracture were observed (Fig. 12(c) and (d)), and nearly no GNS with tearing interface could be observed on the fracture surfaces, indicating the good bonding of the direct Gr-Al interfaces without amorphous Al_2O_3 intermediate layer.

In summary, for the GNS/Al composites fabricated by wet-mixing and powder metallurgy route, the Gr-Al interfaces played a significant role in strengthening the composites. Although GNS could be well dispersed and aligned for the forged composites, no strengthening could be achieved due to the weak bonding of Gr-Al interfaces with amorphous Al_2O_3 intermediate layer. By using extrusion, the Al_2O_3 layer between

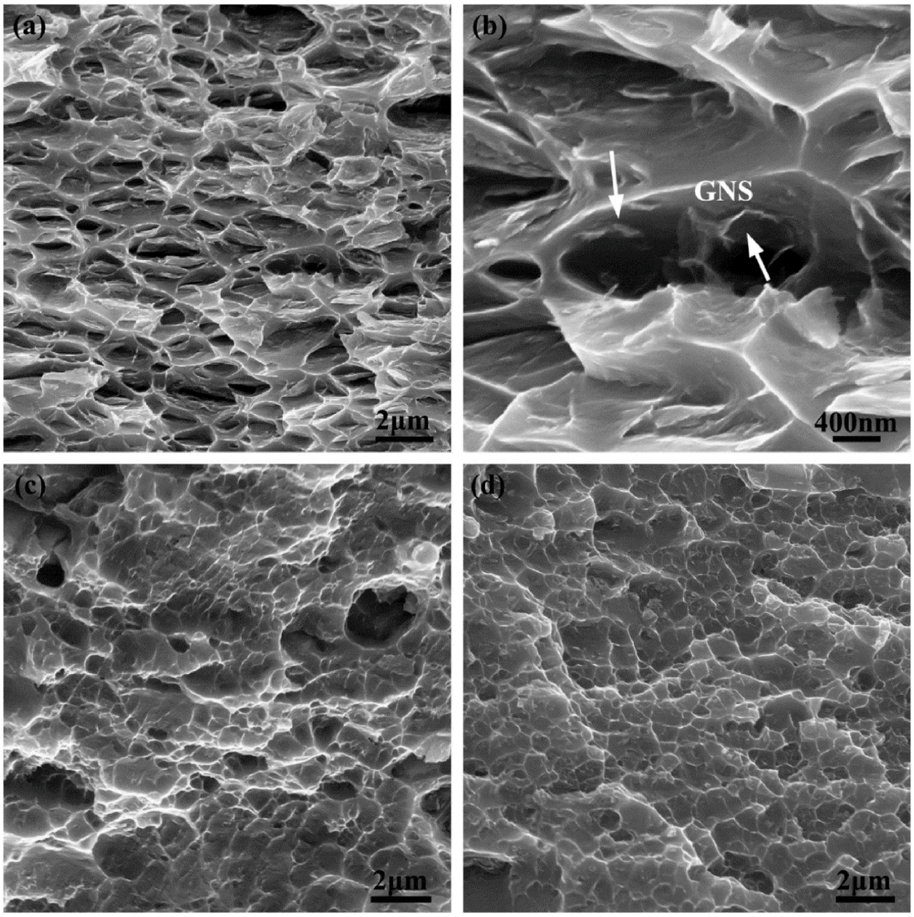

Fig. 12. SEM fractographs: (a) (b) forged GNS/Al–4Cu, (c) forged GNS/Al–4Cu–1Mg and (d) extruded GNS/Al–4Cu.

GNS and Al could partly be fractured, part of the direct Gr-Al interface without amorphous Al_2O_3 intermediate layer could be achieved, and thus strength especially the YS increased significantly compared with those of the alloy matrix. By adding Mg, the Al_2O_3 layer between GNS and Al could be totally exhausted, the direct Gr-Al interface with high shear strength could be achieved, and the best strengthening efficiency was obtained as a result.

5. Conclusions

GNS/Al composite powders with good structural integrity and uniformly dispersed GNS were successfully obtained by wet mixing of GO aqueous solution and flaky Al powders, and subsequent thermal reduction. Then, forged GNS/Al–4Cu, extruded GNS/Al–4Cu and forged GNS/Al–4Cu–1Mg composites with 0.3 vol% GNS were successfully fabricated in different powder metallurgy routes.

For the forged GNS/Al–4Cu composite, the amorphous Al_2O_3 intermediate layers were observed at the Gr-Al interfaces, resulting in weak bonding of Gr-Al ($[\tau]\sim117$ MPa, $[\sigma]\sim227$ MPa). As a result, nearly no strengthening effect was achieved by GNS addition. Subsequent extrusion on hot-pressed GNS/Al–4Cu composite could partly break the Al_2O_3 layers between GNS and Al matrix, and therefore led to improved Gr-Al interface. Therefore, enhanced strengthening effect was achieved.

The amorphous Al_2O_3 intermediate layers in the Gr-Al interfaces were completely exhausted by Mg addition, leading to the direct Gr-Al interface with high shear strength ($[\tau]\sim209$ MPa, $[\sigma]\sim402$ MPa). Therefore, the highest strengthening efficiency of GNS with strengthening factor of ~33 was achieved in the forged GNS/Al–4Cu–1Mg composite.

Author statement

All authors contribute substantially to the paper. Zhenyu Liu (first author) carried out the data collection, data analysis and manuscript writing; Lihong Wang fabricated the composites and tested the tensile properties; Yuning Zan, Wenguang Wang helped to analyze the microstructure; Bolv Xiao designed the experiment and provided the fund; Quanzhao Wang, Dong Wang and Dingrui Ni participated in the design of experiment and analysis of the experimental data; Zongyi Ma revised the manuscript and provided the fund. All authors read and approved the final manuscript.

Declaration of competing interest

The authors declare that they have no known competing financial interests or personal relationships that could have appeared to influence the work reported in this paper.

Acknowledgements

The authors gratefully acknowledge the support of (a) National Key R & D Program of China (No. 2017YFB0703104); Key Research Program of Frontier Sciences, CAS (NO. QYZDJ-SSW-JSC015); (b) the National Natural Science Foundation of China (No. 51501189); (c) the Youth Innovation Promotion Association CAS (2020197).

References

[1] Tjong SC. Recent progress in the development and properties of novel metal matrix nanocomposites reinforced with carbon nanotubes and graphene nanosheets. Mater Sci Eng R Rep 2013;74:281–350.

[2] Xie Y, Meng X, Huang Y, Li J, Cao J. Deformation-driven metallurgy of graphene nanoplatelets reinforced aluminum composite for the balance between strength and ductility. Composites Part B 2019;177:107413.

[3] Srivastava AK, Gupta V, Yerramalli CS, Singh A. Flexural strength enhancement in carbon-fiber epoxy composites through graphene nano-platelets coating on fibers. Composites Part B 2019;179:107539.

[4] Ferreira F, Ferreira I, Camacho E, Lopes F, Marques AC, Velhinho A. Graphene oxide-reinforced aluminium-matrix nanostructured composites fabricated by accumulative roll bonding. Composites Part B 2019;164:265–71.

[5] Zhang ZW, Liu ZY, Xiao BL, Ni DR, Ma ZY. High efficiency dispersal and strengthening of graphene reinforced aluminum alloy composites fabricated by powder metallurgy combined with friction stir processing. Carbon 2018;135:215–23.

[6] Zhang X, Shi CS, Liu EZ, Zhao NQ, He CN. High-strength graphene network reinforced copper matrix composites achieved by architecture design and grain structure regulation. Mater Sci Eng 2019;762:138063.

[7] Youbin K, Jinsup L, Min Sun Y, Jae Won S, Hyungjun K, Yi C, et al. Strengthening effect of single-atomic-layer graphene in metal-graphene nanolayered composites. Nat Commun 2013;4. 2114: 1-7.

[8] Jin B, Xiong DB, Tan Z, Fan G, Guo Q, Su Y, et al. Enhanced corrosion resistance in metal matrix composites assembled from graphene encapsulated copper nanoflakes. Carbon 2019;142:482–90.

[9] Hwang J, Yoon T, Jin SH, Lee J, Kim T-S, Hong SH, et al. Enhanced mechanical properties of graphene/copper nanocomposites using a molecular-level mixing process. Adv Mater 2013;25(46):6724–9.

[10] Li M, Che H, Liu X, Liang S, Xie H. Highly enhanced mechanical properties in Cu matrix composites reinforced with graphene decorated metallic nanoparticles. J Mater Sci 2014;49(10):3725–31.

[11] Liu ZY, Ma K, Fan GH, Zhao K, Zhang JF, Xiao BL, Ma ZY. Enhancement of the strength-ductility relationship for carbon nanotube/Al–Cu–Mg nanocomposites by material parameter optimisation. Carbon 2020;157:602–13.

[12] Choi HJ, Shin JH, Bae DH. The effect of milling conditions on microstructures and mechanical properties of Al/MWCNT composites. Composites Part A 2012;43(7):1061–72.

[13] Esawi AMK, Morsi K, Sayed A, Taher M, Lanka S. The influence of carbon nanotube (CNT) morphology and diameter on the processing and properties of CNT-reinforced aluminium composites. Composites Part A 2011;42(3):234–43.

[14] Liu ZY, Xiao BL, Wang WG, Ma ZY. Modelling of carbon nanotube dispersion and strengthening mechanisms in Al matrix composites prepared by high energy ball milling-powder metallurgy method. Composites Part A 2017;94:189–98.

[15] Shin SE, Choi HJ, Shin JH, Bae DH. Strengthening behavior of few-layered graphene/aluminum composites. Carbon 2015;82:143–51.

[16] Kim WJ, Lee TJ, Han SH. Multi-layer graphene/copper composites: preparation using high-ratio differential speed rolling, microstructure and mechanical properties. Carbon 2014;69:55–65.

[17] Pérez-Bustamante R, Bolaños-Morales D, Bonilla-Martínez J, Estrada-Guel I, Martínez-Sánchez R. Microstructural and hardness behavior of graphene-nanoplatelets/aluminum composites synthesized by mechanical alloying. J Alloys Compd 2014;615:S578–82.

[18] Tabandeh-Khorshid M, Kumar A, Omrani E, Kim C, Rohatgi P. Synthesis, characterization, and properties of graphene reinforced metal-matrix nanocomposites. Composites Part B 2020;183:107664.

[19] Zhou W, Mikulova P, Fan Y, Kikuchi K, Nomura N, Kawasaki A. Interfacial reaction induced efficient load transfer in few-layer graphene reinforced Al matrix composites for high-performance conductor. Composites Part B 2019;167:93–6.

[20] Li Z, Fan G, Tan Z, Guo Q, Xiong D, Su Y, et al. Uniform dispersion of graphene oxide in aluminum powder by direct electrostatic adsorption for fabrication of graphene/aluminum composites. Nanotechnology 2014;25:325601–9.

[21] Lakshmi Dasari B, Morshed M, Nouri JM, Brabazon D, Naher S. Mechanical properties of graphene oxide reinforced aluminium matrix composites. Composites Part B 2018;145:136–44.

[22] Jiang Y, Xu R, Tan Q, Ji G, Fan G, Li Z, et al. Interface-induced strain hardening of graphene nanosheet/aluminum composites. Carbon 2019;146:17–27.

[23] Li Z, Guo Q, Li ZQ, Fan GL, Xiong DB, Su YS, et al. Enhanced mechanical properties of graphene (reduced graphene oxide)/aluminum composites with a bioinspired nanolaminated structure. Nano Lett 2015;15(12):8077–83.

[24] Wang K, Wang Y, Fan Z, Yan J, Wei T. Preparation of graphene nanosheet/alumina composites by spark plasma sintering. Mater Res Bull 2011;46(2):315–8.

[25] Wu GH, Yu ZH, Jiang LT, Zhou C, Deng G, et al. A novel method for preparing graphene nanosheets/Al composites by accumulative extrusion-bonding process. Carbon 2019;152:932.

[26] Hahm MG, Nam J, Choi M, Park CD, Cho B, Kazunori S, et al. Low interfacial contact resistance of Al-graphene composites via interface engineering. Nanotechnology 2015;26(21):215603.

[27] Liu J, Khan U, Coleman J, Fernandez B, Rodriguez P, Naher S, et al. Graphene oxide and graphene nanosheet reinforced aluminium matrix composites: powder synthesis and prepared composite characteristics. Mater Des 2016;94:87–94.

[28] Rashad M, Pan F, Tang A, Asif M. Effect of Graphene Nanoplatelets addition on mechanical properties of pure aluminum using a semi-powder method. Prog Nat Sci 2014;24(2):101–8.

[29] Zan YN, Zhou YT, Zhao H, Liu ZY, Wang QZ, Wang D, et al. Enhancing high-temperature strength of ($B_4C+Al_2O_3$)/Al designed for neutron absorbing materials by constructing lamellar structure. Composites Part B 2020;183:107674.

[30] Zhao K, Liu ZY, Xiao BL, Ma ZY. Friction stir welding of carbon nanotubes reinforced Al-Cu-Mg alloy composite plates. J Mater Sci Technol 2017;33:1004–8.

[31] Liu ZY, Xiao BL, Wang WG, Ma ZY. Analysis of carbon nanotube shortening and composite strengthening in carbon nanotube/aluminum composites fabricated by multi-pass friction stir processing. Carbon 2014;69:264–74.

[32] Choi HJ, Shin JH, Min BH, Park JS, Bae DH. Reinforcing effects of carbon nanotubes in structural aluminum matrix nanocomposites. J Mater Res 2009;24(28):2610–6.

[33] Bhingole PP, Chaudhari GP, Nath SK. Processing, microstructure and properties of ultrasonically processed in situ $MgO\text{-}Al_2O_3\text{-}MgAl_2O_4$ dispersed magnesium alloy composites. Composites Part A 2014;66:209–17.

[34] Li YZ, Wang QZ, Wang WG, Xiao BL, Ma ZY. Interfacial reaction mechanism between matrix and reinforcement in B_4C/6061Al composites. Mater Chem Phys 2015;154:107–17.

[35] Jeong YJ, Cha SI, Kim KT, Lee KH, Mo CB, et al. Synergistic strengthening effect of ultrafine-grained metals reinforced with carbon nanotubes. Small 2007;3(5):840–4.

[36] Liu ZY, Xiao BL, Wang WG, Ma ZY. Effect of carbon nanotube orientation on mechanical properties and thermal expansion coefficient of carbon nanotube-reinforced aluminum matrix composites. Acta Metall Sin 2014;27:901–8. 05.

[37] Shin SE, Choi HJ, Hwang JY, Bae DH. Strengthening behavior of carbon/metal nanocomposites. Sci Rep 2015;5(1–7):16114.

[38] Lewin E, Persson POA, Lattemann M, Stuber M, Gorgoi M, Sandell, et al. On the origin of a third spectral component of C1s XPS-spectra for nc-TiC/a-C nanocomposite thin films. Surf Coating Technol 2008;202:3563–70.

[39] Liu Z, Zhang SM, Yang JR, Liu JZ, Yang YL, Zheng QS. Interlayer shear strength of single crystalline graphite. Acta Mech Sin 2012;28:978–82.

[40] Bonelli F, Manini N, Cadelano E, Colombo L. Atomistic simulations of the sliding friction of graphene flakes. Eur Phys J B 2009;70:449–59.

[41] Guo Y, Guo W, Chen C. Modifying atomic-scale friction between two graphene sheets: a molecular-force-field study. Phys Rev B 2007;76:155429.

[42] Ding XD, Wang YZ, Xiong XM, Du XS, Zhang JX. Measurement of shear strength for Hopg with scanning tunneling microscopy by thermal excitation method. Ultramicroscopy 2012;115:1–6.

[43] Porwal H, Tatarko P, Grasso S, Khaliq J, Dlouhý I, Reece MJ. Graphene reinforced alumina nano-composites. Carbon 2013;64:359–69.

[44] Zan YN, Zhang Q, Zhou YT, Liu ZY, Wang QZ, Wang D, Xiao BL, Ren WC, Ma ZY. Introducing graphene (reduced graphene oxide) into Al matrix composites for enhanced high-temperature strength. Composites Part B 2020;195:108095.